

Direct measurement of the Criegee intermediate CH_2OO in ozonolysis of ethene

Received: 18 October 2024

Accepted: 1 July 2025

Published online: 15 July 2025

Mixtli Campos-Pineda ^{1,3,4}, Lei Yang ^{1,4} & Jingsong Zhang ^{1,2} 

The transient species produced from reactions of unsaturated hydrocarbons with ozone, carbonyl oxides, termed “Criegee intermediates”, play a key role in tropospheric oxidation mechanisms. Direct observation and characterization of Criegee intermediates in ozonolysis *in situ* were proven difficult in decades of efforts. Here, we report the direct measurement of the simplest Criegee intermediate, CH_2OO , from ozonolysis of ethene by cavity ring-down spectroscopy in a flow cell reactor. The transient CH_2OO is quantified rapidly by near-ultraviolet absorption spectra via its $\tilde{\text{B}}(^1\text{A}') \leftarrow \tilde{\text{X}}(^1\text{A}')$ transition. Time profiles of CH_2OO produced in ozonolysis under quasi-steady state conditions are observed. These CH_2OO concentration profiles benchmark the modeling of the ethene ozonolysis reaction network and mechanism, allowing for determination of the yield and various kinetic data of CH_2OO .

Ozonolysis of olefins plays an important role in the troposphere as it is one of the main oxidation processes of unsaturated volatile organic carbons^{1–3}. Products of ozonolysis can ultimately lead to the production of highly oxidized molecules, secondary organic aerosols, carbonyl products, organic radicals, and hydroxyl radical^{4–7}. The oxidizing capacity of this reaction lies in its mechanism, first described in the liquid phase by Rudolph Criegee⁸, which involves a 1,3 dipolar cycloaddition of ozone to the olefinic bond, through a van der Waals complex, leading to the formation of a primary ozonide (POZ)^{9,10}. This reaction is highly exothermic and the POZ breaks rapidly into a carbonyl and a carbonyl oxide product with broad internal energy distributions. The carbonyl oxide product, also known as Criegee intermediate (CI), is a transient species that is involved in the oxidation processes mentioned above either via isomerization, decomposition, or bimolecular reactions. Carbonyl oxides with low internal energy will have a long enough lifetime to undergo bimolecular reactions and are called “stabilized” Criegee intermediates (sCIs)^{11–14}, whereas highly energetic carbonyl oxides are known as “hot” CIs.

For decades, Criegee intermediates have been the subject of extensive studies. The breakthrough work of Welz et al.¹⁵ devised a method for the synthesis of sCIs by photolysis of diiodoalkanes and subsequent reaction of the iodoalkyl radicals with oxygen. This method has been exploited by many groups to measure ultraviolet^{16–18} and infrared¹⁹ spectra, study fundamental unimolecular processes^{20,21},

and determine kinetic rate constants for several bimolecular reactions of atmospheric interest^{15,22–25}. The first of the carbonyl oxides studied in this manner was formaldehyde oxide, CH_2OO ¹⁵, leading to extensive kinetic information on its bimolecular reactions^{15,22,23}, as well as its unimolecular decomposition and isomerization processes^{16,24}. However, due to the highly exothermic POZ decomposition following 1,3 dipolar cycloaddition of ozone to the olefinic bond, the production of Criegee intermediates in ozonolysis is accompanied by high internal energy^{9,26,27}. Experimental studies of ethene ozonolysis and theoretical computations of the energetics of formaldehyde oxide produced from the scission of the POZ show that the nascent yield of “stabilized” CH_2OO is 0.20 (± 0.003)^{11,12,28}, while it increases to 0.42 (± 0.1) at atmospheric pressure due to collisional stabilization²⁹. In addition, its low OH yield (0.17 ± 0.05)^{29,30} is strong evidence that the absence of α -hydrogens leads to isomerization of the “hot” CI into dioxirane, and its subsequent processes lead to fragments that participate in further reactions. Hence, both the “hot” and “stabilized” fractions of CH_2OO add to the complexity of the ozonolysis mechanism, and more information on this branching and the secondary processes becomes important for a better understanding of the ozonolysis reaction in the troposphere³¹. Therefore, it is necessary to study the ozonolysis reaction itself by monitoring the important species and comparing experimental measurements with a model mechanism that contains accurate pathways and rate constants. CIs, as the immediate fragment

¹Department of Chemistry, University of California, Riverside, CA, USA. ²Air Pollution Research Center, University of California, Riverside, CA, USA. ³Present address: Centre for Research into Atmospheric Chemistry, University College, Cork, Ireland. ⁴These authors contributed equally: Mixtli Campos-Pineda, Lei Yang. ✉ e-mail: jingsong.zhang@ucr.edu

of POZ that determine the reaction branching and connect to subsequent reaction pathways in ozonolysis, control the outcomes of the ozonolysis reactions and are thus the most crucial transient species in ozonolysis. Direct observation and kinetic measurements of CIs in ozonolysis in situ in real time will anchor the reaction mechanisms and greatly improve our fundamental understanding of the whole reaction network.

Decades of efforts have proven the difficulty in measuring Criegee intermediates directly from gas-phase ozonolysis in situ due to their transient nature, high reactivity, and low concentrations (from slow production and fast reactions and decomposition)^{32,33}. Recently, Womack et al.³³ reported the first direct observation of CH₂OO in ozonolysis of ethene using the subtle signals attributed to CH₂OO measured by Fourier transform microwave spectroscopy and pulsed nozzle over a very long time signal integration (4.3 h or 93,000 sample injections) but at only one poorly-defined residence time (estimated to be <0.5 s with a 6-Hz sampling rate). In this work, we couple a flow cell reactor with cavity ring-down spectroscopy (CRDS) and exploit the high sensitivity of the multi-pass absorption spectroscopy technique to directly observe and measure kinetics of the transient CH₂OO intermediate in ozonolysis of ethene at short residence times. The measured near-ultraviolet (near-UV) spectra are compared to a literature reference spectrum of CH₂OO, allowing for determination of the number densities. The strong absorption features of CH₂OO with good signal-to-noise ratios facilitate direct kinetic and mechanistic studies with time profiles of CH₂OO in actual ozonolysis systems. Time-dependent concentrations of HCHO product and consumed O₃ are also determined similarly in separate measurements under the same reaction conditions. A mechanism of ethene ozonolysis is constructed with available kinetic data and constrained with the measured time-dependent number densities to assess the best-fit kinetic rate constants of reactions that are important secondary steps in the ozonolysis of alkenes. The detailed experimental and kinetic simulation methods are described in Method Section and supplementary materials.

Results

Detection of CH₂OO

Figure 1 shows the high-resolution absorption spectrum of CH₂OO in situ from ethene ozonolysis, where the absorption cross-sections were scaled from measured absorption coefficient in comparison with CH₂OO reference spectra by Foreman et al.³⁴. Under the reaction condition of this spectrum in the region of 363–395 nm (initial ozone concentration of $1.8 \times 10^{15} \text{ cm}^{-3}$, initial ethene concentration of $1 \times 10^{17} \text{ cm}^{-3}$, residence time of ~140 ms, and pressure of 10 Torr), all the absorptions except that from CH₂OO were considered negligible, and the number density of CH₂OO was determined to be $2.75 \times 10^{11} \text{ cm}^{-3}$. Note that the residence time in the plug flow reactor here represents reaction times spanning from 0 to the nominal total residence time (e.g., the 140 ms residence time represents reaction times from 0 to 140 ms), with the measurement integrating the signal from the point of injection up to the nominal total residence time, probing an average across a horizontal slice in Supplementary Fig. 1. The spectral resolution in this work (0.01 nm) is higher compared to those in the references (~0.12–2 nm)^{16–18,34,35}. Vibronic bands of the $\tilde{B}^1(A') \leftarrow \tilde{X}^1(A')$ transition of CH₂OO, which originate from excitation to the bound levels of the \tilde{B} state rather than from hot bands³⁴, show excellent agreement with the reference spectra^{17,34,35}. The good signal-to-noise ratio in this work allowed the determination of CH₂OO concentration using the vibronic band features spaced by ~8 nm (or 600 cm⁻¹) with half-peak widths of ~3.5 nm (or 200 cm⁻¹) in the following kinetic experiments. The relative uncertainties in CH₂OO absorption cross sections in the references listed (15–30%^{17,34,35}) are larger than our spectra uncertainties (1 σ error bar estimated to be ~3–10% from repeated measurements, see Source Data for Fig. 3), therefore the

uncertainties of the cross sections determined in this work by scaling to the reference cross sections from Foreman et al. are ~30%³⁴ and could be improved when more accurate CH₂OO reference become available in the future. HCHO was not produced in high enough concentration in the short residence times to affect the absorption spectra of CH₂OO in 363–395 nm. Only when residence time and reactant concentrations were increased by more than 10 times, weak rovibronic features from the $\tilde{a}^3A_2 \leftarrow \tilde{X}^1A_1$ transition of HCHO^{36,37} can be identified in this wavelength region (see Supplementary Fig. 2). This confirms that residence times smaller than 500 ms were short enough to avoid spectra interference from other reaction byproducts along the reaction cell.

Further confirmation that the absorption features observed belong to CH₂OO was obtained by adding sulfur dioxide to the ozonolysis reaction via the C₂H₄ + N₂ flow to scavenge CH₂OO with a rate constant of $3.7 (\pm 0.5) \times 10^{-11} \text{ cm}^3 \text{ s}^{-1}$ ⁽²⁹⁾. The concentration of SO₂ used was $9 \times 10^{14} \text{ cm}^{-3}$, more than a thousandfold the concentration of CH₂OO. Figure 2 shows the change in absorption coefficient for the ozonolysis reaction with and without SO₂. With the addition of SO₂, the features attributed to CH₂OO vanish and only the spectra of SO₂ remain. This chemical titration is a strong indication that the absorption features observed indeed belong to CH₂OO. Supplementary Fig. 3 further shows that the CH₂OO concentration decreased by more than 95% after the excess amount of SO₂ was added.

Ethene and ozone were introduced to the flow reactor in excess concentrations, becoming the main drivers of the chemical processes. Therefore, the rate constants of their reactions with CH₂OO can be measured with some degree of precision. Residence time gradually increased from 9 to 434 ms and the average concentrations of CH₂OO in the flow reactor were measured. Figure 3 illustrates the concentrations of CH₂OO from experiments conducted at various residence times and under different ethene and ozone concentrations (depicted by solid symbols) at 10 Torr, showing clear production and depletion time profiles that are modeled and compared to kinetic simulation (represented by open symbols; discussed next). The time profiles (9–434 ms residence time) of Criegee intermediate produced in

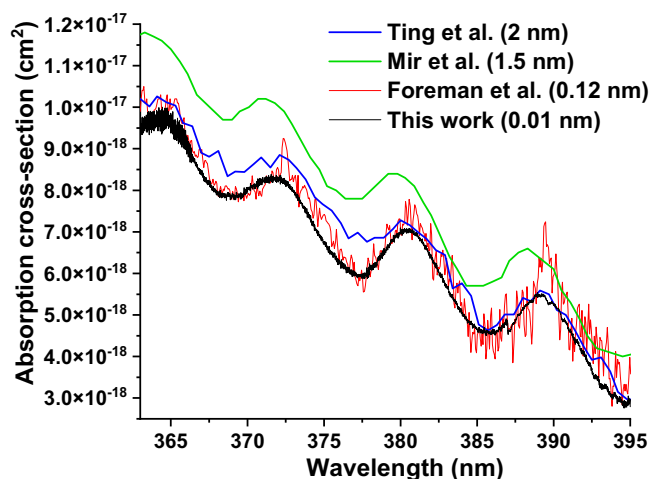


Fig. 1 | Absorption cross-sections of the 363–395 nm section of the $\tilde{B}^1(A') \leftarrow \tilde{X}^1(A')$ transition of CH₂OO produced in ethene ozonolysis. The reaction conditions were initial ozone concentration of $1.8 \times 10^{15} \text{ cm}^{-3}$, initial ethene concentration of $1 \times 10^{17} \text{ cm}^{-3}$, and residence time of ~140 ms. The laser scanning step was 0.01 nm. The cross-sections in this work (in black) were determined by scaling the absorption coefficient to the reference cross-section data from Foreman et al.³⁴ (in red), and compared to Ting et al.¹⁷ (in blue) and Mir et al.³⁵ (in green), adapted with permission from American Chemical Society and Royal Society Chemistry. The resolution of the reference spectra are labeled. Source data are provided as a Source Data file.

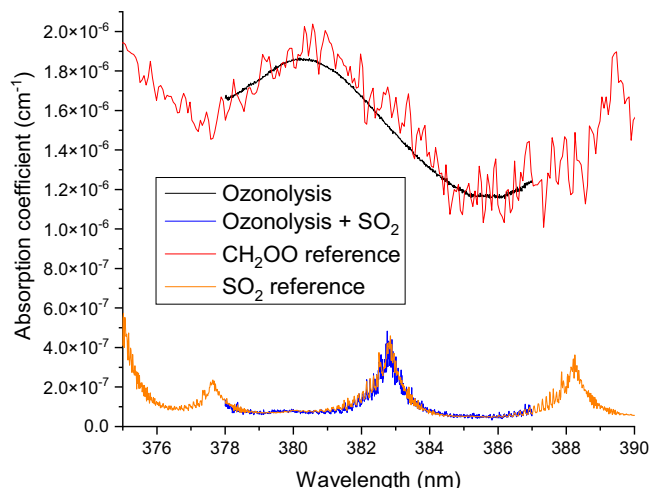


Fig. 2 | Absorption spectra measured during ozonolysis of ethene with the presence (in blue) and absence (in black) of high-concentration SO_2 (used as a scavenger). The CH_2OO concentration decreased by more than 95% after the addition of the scavenger (see enlarged Supplementary Fig. 3). The SO_2 reference spectra (Vandaele et al.⁷⁷, in orange) were obtained from the MPI-Mainz UV/VIS Spectral Atlas⁶². The CH_2OO reference (in red) was scaled from cross-section data of Foreman et al.³⁴ Source data are provided as a Source Data file.

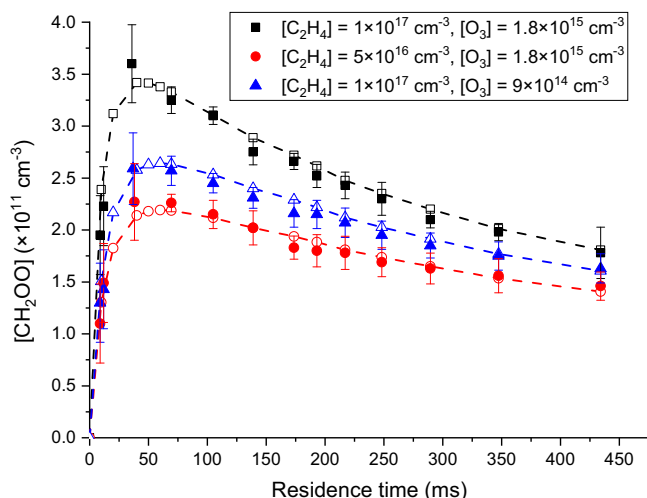


Fig. 3 | Concentration time profile of CH_2OO in ethene ozonolysis at different flow rates (residence times) under different reaction conditions at 10 Torr and 293 K. (solid symbols: experimental data; open symbols: kinetic simulation; black squares: initial ethene concentration $[\text{C}_2\text{H}_4] = 1 \times 10^{17} \text{ cm}^{-3}$ and initial ozone concentration $[\text{O}_3] = 1.8 \times 10^{15} \text{ cm}^{-3}$; red circles: $[\text{C}_2\text{H}_4] = 5 \times 10^{16} \text{ cm}^{-3}$ and $[\text{O}_3] = 1.8 \times 10^{15} \text{ cm}^{-3}$; blue triangles: $[\text{C}_2\text{H}_4] = 1 \times 10^{17} \text{ cm}^{-3}$ and $[\text{O}_3] = 9 \times 10^{14} \text{ cm}^{-3}$). The dashed lines connect the kinetic simulation open symbols under the different reaction conditions. The concentration of CH_2OO at 174 ms with $[\text{C}_2\text{H}_4] = 1 \times 10^{17} \text{ cm}^{-3}$ and $[\text{O}_3] = 1.8 \times 10^{15} \text{ cm}^{-3}$ was measured three times for the 1 σ error bar, while spectra baseline fluctuations were used to estimate the error bars of other data points. Source data are provided as a Source Data file.

ozonolysis were observed. Notably, the CH_2OO concentration quickly ascends from zero upon the mixing of ethene and ozone. Subsequently, the interplay of bimolecular reactions and (to a lesser extent) unimolecular decomposition of sCIs becomes evident in consuming CH_2OO , making the net production of CH_2OO slow down and reach its maximum concentration around 40–60 ms. Beyond the inflection point, the consumption rates of CH_2OO surpass its production, leading to a steady decline in the concentration of CH_2OO over the longer

residence times. The concentration of CH_2OO at 174 ms with relatively high alkene and high ozone concentrations (solid black square) was measured three times to generate the 1 σ error bar ($8 \times 10^9 \text{ cm}^{-3}$) at that point, while spectra baseline fluctuations ($\Delta\alpha$) were used to estimate the error bars of other data points ($\sim 1\text{--}3 \times 10^{10} \text{ cm}^{-3}$) in Fig. 3 (assuming no additional uncertainties from the CH_2OO reference). The changes in absorption spectra of the three kinetic curves are shown in Supplementary Fig. 4.

Reaction network simulation and reaction mechanism

Prior to the experiments, a preliminary kinetic simulation was first built and utilized to optimize the initial experimental conditions for CH_2OO production at different residence times. It was further revised later after comparison with the experimental measurements. The plug flow reactor model was validated with parameters listed in Supplementary Table 1 and simulated as a series of continuous stirred tank reactors (CSTR), where the output of a CSTR becomes the input of the next one along the flow cell. A full description of the revised kinetic model and ethene ozonolysis mechanism can be found in Supplementary Table 2, and a simplified schematic mechanism is in Fig. 4. Supplementary Table 3 summarizes and compares the pseudo-first-order reaction rates of CH_2OO consumption reactions at 10 ms and 434 ms residence time. At the beginning stage of 10 ms, the reactions with O_3 and ethene are the major consumption pathways ($\sim 56\%$ and $\sim 14\%$) of CH_2OO . The bimolecular self-reaction of CH_2OO also plays an important role ($\sim 25\%$) due to its fast reaction rate constant ($7.40 \times 10^{-11} \text{ cm}^3 \text{ s}^{-1}$). As the reaction goes on, byproducts produced in ozonolysis and secondary reactions accumulate and gradually become important consumption pathways of CH_2OO . At 434 ms, the reactions with HCHO , HCOOH (from $\text{CH}_2\text{OO} + \text{HCHO}$), and O_3 are the major reactions of CH_2OO , taking up to $\sim 45\%$, $\sim 21\%$, and $\sim 17\%$ of its consumption, respectively. From 10 ms to 434 ms, the total pseudo-first-order consumption rate of CH_2OO increases from 139 s^{-1} to 452 s^{-1} , illustrating that it is important to keep residence time short to maximize the concentration of CH_2OO . The plot of percentage contributions to CH_2OO loss as a function of residence time is presented in Supplementary Fig. 5. Supplementary Fig. 1 depicts the concentration profile of CH_2OO along the reactor at various residence times within the 500 ms timeframe, obtained from kinetic simulation conducted with the initial ethene and ozone concentrations of 1×10^{17} and $1.8 \times 10^{15} \text{ cm}^{-3}$, respectively. This contour plot also underscores the importance of maintaining a short residence time to guarantee a sufficiently detectable concentration of CH_2OO .

Rate constants of most of the bimolecular reactions of CH_2OO that play a role in the ozonolysis mechanism were obtained from kinetic studies of CH_2OO found in the literature, as explained above. An exception is the rate constant of the CH_2OO reaction with C_2H_4 ($k = 7 (\pm 1) \times 10^{-16} \text{ cm}^3 \text{ s}^{-1}$) measured by Buras et al.²⁵ In their work they suggested this rate constant to be considered as a lower limit. Theoretical calculation by Sun et al.³⁸ found the rate constant to be higher ($3.91 \times 10^{-15} \text{ cm}^3 \text{ s}^{-1}$). However, we found the best fit of the model when the rate constant of $\text{CH}_2\text{OO} + \text{C}_2\text{H}_4$ was set to $2 (\pm 0.2) \times 10^{-16} \text{ cm}^3 \text{ s}^{-1}$ in order to account for the difference in the average concentration of CH_2OO when the total rate of production is kept the same but the ratio of C_2H_4 and O_3 changes. Error analysis was performed by randomly varying corresponding rate constants 100 times assuming a Gaussian distribution to generate the 1 σ standard deviations, as shown with the error bars in kinetic simulation (colored shades) in Supplementary Fig. 6. The upper limits of the error bars of kinetic data were confirmed when the modeling results apparently mismatched with the experimental trends. The experimental data also indicate that the rate constant of the reaction of CH_2OO and O_3 must be higher than that for CH_2OO and C_2H_4 as more CH_2OO remains when the initial concentration of ozone decreases, indicating that ozone contributes more to CH_2OO depletion. The

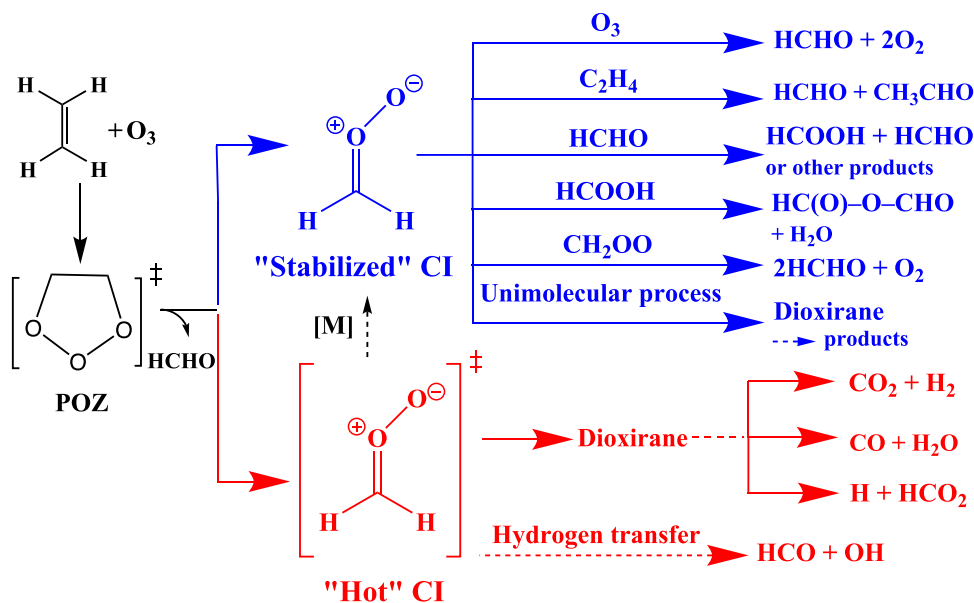


Fig. 4 | Simplified reaction network of ethene ozonolysis under laboratory condition, emphasizing primary reaction channels of “stabilized” and “hot” CH_2OO . Detailed reaction mechanism is in Supplementary Table 2.

best fit to experimental data occurs when the rate constant of the reaction of CH_2OO with O_3 is set to $4.5 (\pm 0.5) \times 10^{-14} \text{ cm}^3 \text{ s}^{-1}$. Theoretical work from Vereecken et al.^{39,40} obtained a rate constant of $4 \times 10^{-13} \text{ cm}^3 \text{ s}^{-1}$. Experimental work by Onel et al.⁴¹ reported this rate constant to be $3.6 (\pm 0.8) \times 10^{-13} \text{ cm}^3 \text{ s}^{-1}$. However, in our ethene ozonolysis mechanism, it was found that a rate constant higher than $2 \times 10^{-13} \text{ cm}^3 \text{ s}^{-1}$ would completely inhibit the nonlinear behavior in the depletion of CH_2OO at longer residence times, as ozone would become the only important depletion process. Copeland et al.⁴² find their data to be best fitted with a rate constant of $\text{CH}_2\text{OO} + \text{O}_3$ of $1 \times 10^{-13} \text{ cm}^3 \text{ s}^{-1}$. Chang et al.⁴³ reported a rate constant of $6.7 (\pm 0.8) \times 10^{-14} \text{ cm}^3 \text{ s}^{-1}$. Our best-fit rate is more consistent with that by Chang et al.⁴³.

As a main product of ethene ozonolysis, formaldehyde also drives secondary chemical processes and is likely to account for the nonlinear depletion of CH_2OO in our experiments. Copeland et al.⁴² used product branching ratios of the $\text{CH}_2\text{OO} + \text{HCHO}$ to obtain a best-fit total rate constant of $9.2 \times 10^{-13} \text{ cm}^3 \text{ s}^{-1}$. However, our best fit occurs when the total rate constant is set to $3.1 (\pm 0.3) \times 10^{-12} \text{ cm}^3 \text{ s}^{-1}$. Recently, Luo et al.⁴⁴ reported this rate constant to be $4.11 (\pm 0.25) \times 10^{-12} \text{ cm}^3 \text{ s}^{-1}$, showing consistency with our result. In addition, our model shows only slight differences in the average concentrations of CH_2OO when different branching ratios are used for the different pathways of CH_2OO with formaldehyde, preventing any meaningful assignment of its branching ratios in our model. More work is, therefore, needed to assess the depletion of CH_2OO by HCHO , and the importance of its reaction products in subsequent reaction pathways.

From the fitting of kinetic modeling with the experimental $[\text{CH}_2\text{OO}]$ data, the yield of stabilized CH_2OO was determined to be $0.25 (\pm 0.07)$ in the low-pressure region (~ 10 Torr). The error bar of the sCI yield from kinetic simulation (relative error $\sim 4\%$, see Supplementary Fig. 6) was much smaller than the uncertainty of $[\text{CH}_2\text{OO}]$ originated from the CH_2OO reference spectra (relative error $\sim 30\%$), with the latter contributing to most of the sCI yield uncertainty. Previously, the yield of sCIs in ethene ozonolysis was measured to be ~ 0.19 – 0.25 below 20 Torr using chemical titration reactions of sCIs with excess scavenger SO_2 ^{11,28}. Theoretical studies using statistical models reported the nascent yield of 0.2 at the zero-pressure limit¹², while more recent calculations using both statistical

and trajectory models reported $0.36^{9,26}$. Our result agrees well with the yields from the chemical titration method and the statistical models. When the pressure changed from 4 to 19 Torr, the stabilized CH_2OO yield showed a modest increase (0.23 – 0.25) (± 0.07), consistent with previous studies as shown in Supplementary Fig. 7.

The consumption of ozone and production of HCHO were measured in the 325–340 nm range under the same reaction conditions to measure the concentration and yield of formaldehyde. As illustrated in Supplementary Fig. 8, the experimental data indicate linear increases in HCHO concentration within the residence times (< 500 ms). Optimal agreement between the experimental and kinetic simulation of HCHO concentration was achieved when the primary yield of HCHO was set to 0.88. The yield of HCHO from ozonolysis of ethene, extensively studied in the literature^{4,26,42,45–51}, was found to be around 0.9. The primary yield of HCHO employed in our kinetic model aligns well with the previous studies.

To assess the kinetic rates of the reaction between CH_2OO and SO_2 , the absorption spectra of CH_2OO were measured under different residence times with SO_2 introduced at concentrations ranging from 1×10^{13} to $4 \times 10^{13} \text{ cm}^{-3}$. As depicted in Supplementary Fig. 9, the concentration of CH_2OO from kinetic simulation was compared to the experimental results spanning 170 to 430 ms. The determined best value of $k(\text{CH}_2\text{OO} + \text{SO}_2)$ was $3.9 (\pm 0.8) \times 10^{-11} \text{ cm}^3 \text{ s}^{-1}$, demonstrating good concordance with the literature values obtained through photolysis synthesis methods²⁹. The kinetic data measured in this work suggests that, despite the conjecture that the CIs originated from alkene ozonolysis are produced with higher internal energy^{9,26,52} than those arising from photolysis of diiodoalkanes in excess amount of O_2 ^{15,53}, the reaction rates of the thermally equilibrated CIs are comparable. The constructed reaction network in this study helps validate preceding kinetic investigations. One limitation for the kinetic determinations in this work is that the shortest residence time achieved in the current setup was ~ 10 ms, making it challenging to capture the full-time profile for rapid CH_2OO reactions. For instance, in the $\text{CH}_2\text{OO} + \text{SO}_2$ reaction, the CH_2OO signal would rise and peak within 5 ms^{15,21,54–56}. Achieving a residence time closer to 1 ms would likely require a ~ 10 -fold increase in the pumping speed. Besides, uncertainties in residence time due to flow uniformity or wall losses are expected to be negligible based on the ideal plug flow reactor assessment in Supplementary Table 1, but future studies could further quantify their effects to refine kinetic accuracy.

Discussion

Formaldehyde oxide intermediate produced in ozonolysis of ethene was directly characterized in situ in the reaction network using CRDS. Measurements of the time profiles of the transient CH₂OO intermediate at various initial reactant concentrations allowed for quantitative assessment of the production and loss processes of CH₂OO in ozonolysis. These CH₂OO concentration profiles benchmarked the modeling of the ethene ozonolysis reaction network and mechanism, determining the branching and various kinetic data of CH₂OO and providing deeper insights into the ozonolysis reaction. The use of flow reactor and laboratory scale conditions provides additional control on mixing and reaction conditions and allows for the study of known secondary reactions in the ozonolysis mechanism, offering an intermediate step between the determination of individual rate constants and the application of reaction mechanisms in environmental chamber studies, which ultimately leads to better atmospheric chemistry modeling.

This direct ozonolysis method could serve as a platform for studying other CIs in larger ozonolysis systems (which may not be readily accessible by photolysis synthesis method). This study also opens door for studying reaction mechanisms of other complex systems. It demonstrates that one needs to be able to measure the difficult but key species, and CIs are the epitome of this. It shows that direct measurements of the time profiles of the key intermediates in the reactions in situ anchor the whole reaction network and can provide greater understanding of the reaction mechanisms.

Methods

Flow cell reactor

The flow cell reactor was made of cylindrical quartz tube (57 cm length, 2.2 cm ID, and 2.5 cm OD). The inlets of the flow cell were 0.25–0.38 cm OD quartz tubes, while the outlets were 0.38–2.5 cm OD quartz tubes, used for different flow and pumping speeds. The flows of the reactants were controlled by mass flow controllers (MFCs, Aalborg model GFC17S-EAL6-A0) to maintain continuously stable flow rates. The total pressure inside the flow reactor was precisely monitored by a Cole-Parmer pressure gauge (model EW-68936-00). To achieve different residence times under the same pressure, the total flow rates were varied between 0.4 and 5 sL/min with MFCs of different scales for accurate control. The pumping speed of the vacuum pump (Welch model 1397) was adjusted using an inline valve connected to the flow reactor outlet to keep the pressure constant under different flow rates.

Ethene (99.95%, Matheson) flows were in the 0.1–1.5 sL/min range. Nitrogen (0.2–3 sL/min) worked as a buffer gas to adjust the total pressure and the reactant concentrations. Ozone was generated by an ozone generator (ENALY model 1000BT-12) with an oxygen inlet flow of 0.1–0.4 sL/min. The concentration of ozone in the outlet stream of the ozone generator (before entering the flow cell) was monitored with an ozone monitor (2B Tech model 202) after dilution. By adjusting the voltage of the corona discharge inside the ozone generator, as well as using different flow rates of oxygen inlet, the concentration of ozone before entering the flow reactor was ~2–6%. The flow rate of the ozone and oxygen mixture into the flow reactor was 16–800 sL/min. Ethene and ozone were separately introduced with two different-sized tubes (one inside another) so that they would not mix with each other before entering the flow reactor. At the end of the inlet, the ozone and oxygen mixture in the inner tube (Teflon) encountered the mixture of ethene and nitrogen buffer gas exactly at the entry into the reactor. The ozone concentration inside the flow reactor was further confirmed by measuring its absorption spectra around 330–331 nm using CRDS. To obtain higher ozone concentrations (~10%), a silica gel trap (at ~60 °C) was used to trap ozone from a Welsbach ozone generator (model T-408). Compared to the stable ozone concentration using the ozone generator directly, the ozone concentration from the ozone trap gradually decreased upon use and could last only about 2 h. Therefore,

the ozone trap was only used to maximize HCHO features in 370–390 nm at longer residence times (Supplementary Fig. 2). The rest of the HCHO quantification (lower [HCHO]) was performed around 329 nm (Supplementary Fig. 8).

For the studies on the CH₂OO + SO₂ reaction (Supplementary Fig. 9), an SO₂/nitrogen (~4%) mixture was introduced with a flow rate of 0.2–5 sL/min. The SO₂ concentration inside the reactor was measured with its absorption features around 318 nm using CRDS. For the complete scavenging spectra with SO₂ (Fig. 2 and Supplementary Fig. 3), a flow rate of 75 sL/min SO₂/N₂ mixture was used.

The length of the flow reactor (distance between the inlet and outlet) for most experimental data (residence time >35 ms) was 57 cm, while shorter flow cell was used to reduce the residence time to ~10 ms. The quantification of the residence times was achieved with the precisely measured flow rates and pressure, and further confirmed by negative injection and pulse injection methods⁵⁷.

Cavity ringdown spectroscopy

A flow cell was used as a plug flow reactor (PFR) to carry out the ozonolysis reaction under different conditions. The reaction cell also had the role of an optical cavity, and the average concentrations of species of interest were measured using CRDS. This CRDS experimental apparatus is shown in Supplementary Fig. 10 and has been used for different ozonolysis reactions^{58–60}. Number densities are calculated from the ring-down decay time measurements according to:

$$\alpha = \sum_i \sigma_i(\lambda) N_i + f(\lambda) = \frac{L}{c\ell_s} \left(\frac{1}{\tau} - \frac{1}{\tau_0} \right) \quad (1)$$

where $\sigma_i(\lambda)$ is the absorption cross-section of the i -th species at wavelength λ , N_i is its number density, $f(\lambda)$ is a parametric function to account for broad extinction contributions from the background and unidentified species, $1/\tau_0$ is the decay rate of the empty cell, $1/\tau$ is that of the cell with the sample, ℓ_s is the length of the sample in the cell (57 cm in our flow reactor), L is the length of the cell (100 cm), and c is the speed of light.

An Nd: YAG laser (Continuum Surelite II) at 10 Hz was used to pump a tunable dye laser (Lambda Physik ScanMate) to generate red laser radiation from 650 to 680 nm and 726 to 790 nm with different dyes (DCM, pyridine 1, and styryl 8). Then the high-resolution laser radiation (linewidth ~0.13 cm⁻¹) was introduced into an Inrad Auto-tracker through a BBO doubling crystal to produce near-UV radiation (linewidth ~0.2 cm⁻¹) in the 325–340 nm (for quantifying HCHO⁶¹ and O₃) and 363–395 nm (for CH₂OO in Supplementary Fig. 11) wavelength ranges. High reflectivity mirrors ($R > 99.95\%$) centered at 330 and 370 nm (Layertec model 109121 and 109462) were used to obtain ring-down times of 5–13 microseconds. The Nd: YAG pumped dye laser typically scanned the near-UV wavelength at 0.01 nm/step with 20 laser shots for data averaging at each step. The baseline noise of CRDS in this work was about $1\text{--}6 \times 10^{-8} \text{ cm}^{-1}$ ($\Delta\alpha$), depending on the wavelength used and instrumental conditions. This corresponds to an estimated limit of detection of CH₂OO of $\sim 1 \times 10^{10} \text{ cm}^{-3}$ (at 363–395 nm where effective path length of empty cell is ~4000 m and typical ringdown time is ~13 microseconds), based on the reference absorption cross sections from Foreman et al.³⁴ in the MPI-Mainz UV database⁶². The detection limit of HCHO in Supplementary Fig. 8 was estimated to be $\sim 1 \times 10^{12} \text{ cm}^{-3}$ from the baseline noise ($\sim 6 \times 10^{-8} \text{ cm}^{-1}$) and the 328–330 nm absorption cross sections ($\sim 6 \times 10^{-20} \text{ cm}^2$) from the HCHO reference rovibronic spectra⁶¹.

Reactant concentrations were varied from 9×10^{14} – $1.8 \times 10^{15} \text{ cm}^{-3}$ for ozone and 5×10^{16} – $1 \times 10^{17} \text{ cm}^{-3}$ for ethene. Given the slow production of CI ($k(\text{ethene} + \text{O}_3) = 1.6 \times 10^{-18} \text{ cm}^3 \text{ s}^{-1}$) and the existence of several depletion processes (decomposition, reactions with ethene, ozone, formaldehyde, etc.), short residence times were used to inhibit secondary reactions as much as possible. Our experimental conditions

allowed for residence times ranging from 10 to 500 ms, leading to estimated CH₂OO concentrations of $1\text{--}3.5 \times 10^{11} \text{ cm}^{-3}$, lower than or close to what would be generated by photolysis of diiodomethane and reaction with oxygen ($10^{11}\text{--}10^{13} \text{ cm}^{-3}$)^{21,34,35,41,43,44}. The change in ring-down decay rate $\Delta(1/\tau) = (1/\tau) - (1/\tau_0)$ was measured from 363–395 nm and compared to the reference CH₂OO absorption cross sections. The average number density can be determined using Equation 1, provided that there exist distinct absorption features of CH₂OO.

Kinetic simulation

A kinetic model was constructed, and the software package KINTECUS⁶³ was used to estimate concentrations of each CSTR by integration of the system of ordinary differential equations with a Bulirsch-Stoer method. Briefly, it comprises the ozonolysis reaction^{4,11}, decomposition of the “hot” CI⁴², reactions of the “stabilized” CI^{21–25,39,64–68}, HO_x chemistry^{42,69,70}, radical reactions with ozone and ethene, and reactions of the HOCH₂CH₂ radical produced by the reaction of OH with ethene.

The mechanism of ozonolysis of ethene was constructed based on our previous work²⁸ and expanded to include more secondary chemistry with existing and recent kinetic data from the literature^{4,21,22,24,25,39,64,69–71}. Supplementary Table 2 shows the mechanism used to model the ozonolysis reaction. From the ozonolysis reaction (R1), the branching ratios of the “stabilized” and “hot” Criegee intermediates are explicitly set according to Hatakeyama et al.¹¹ and Yang et al.²⁸. The “hot” CH₂OO will readily decompose and isomerize according to Copeland et al.⁴² and references therein, producing H atom, OH radicals, and other fragments (R2–6). The OH radical and H atom will be involved in chemistry with O₃ and the reactions are included in the model with rate constants from evaluated kinetic data and from Copeland et al.^{42,69,70} (R7–12). The chemistry of H atom and OH radicals with ethylene has been included with rate constants from evaluated kinetic data as well (R13–19). The stabilized fraction of CH₂OO undergoes several bimolecular reactions, as well as unimolecular decomposition. Kinetic studies have been performed with stabilized CH₂OO produced by photolysis of CH₂I₂ and subsequent reaction with O₂ by several groups^{21–25,64}. In the model, those reactions involving products from ethene ozonolysis are added (R20–33). The three major consumption reactions of CH₂OO (with ethene, O₃, and HCHO) are studied by comparing with experimental data while varying corresponding rate constants, and the best-fitting results are presented. The reaction rates of CH₂OO with ethene, O₃, and HCHO have been directly determined with the photolysis method and these kinetic data were used as starting points for fitting the model. The concentrations of all the species in the model were free running after initialization, while the reaction rate constants were varied between different runs. Stabilized CH₂OO can also undergo unimolecular processes and are described in the model based on data from previous studies^{21,54,72–74} and the evaluated kinetic data⁷⁰. The ozonolysis reaction produces water and, while the reaction of CH₂OO with water is slow ($k < 5 \times 10^{-16} \text{ cm}^3 \text{ s}^{-1}$), the rate of CH₂OO with water dimer is much faster ($k = 6.2 \times 10^{-12} \text{ cm}^3 \text{ s}^{-1}$). However, from the equilibrium data between water and water dimer^{65,66}, it was concluded that water dimer formation in the system was not significant. Products of the reaction of CH₂OO with carbonyls and organic acids were obtained from experimental and theoretical information in the literature^{21,22,64,67,68}. The reaction of CH₂OO with SO₂ was added for modeling SO₂ titration experiments to get the reaction rate constant (Supplementary Fig. 9). Ketohydroperoxide (KHP) was recently found to be a minor pathway existing at the starting stage of ozonolysis⁵¹ and its chemistry is also included (R1, R80–82). HO_x plays a role in the ozonolysis mechanism either by having an effect on the HO_x budget or by reacting with secondary products of ozonolysis such as formaldehyde or acetaldehyde. This

chemistry is included in the model (R34–45, R54–65) with rate constants from evaluated kinetic data^{69,70}. Using an ozone generator to produce ozone via corona discharge in a stream of pure oxygen results in high concentrations of oxygen going into the system. Therefore, the secondary chemistry of oxygen has been included in the kinetic model (R46–49, R66–79). The reactions of HO_x with products of ozonolysis indicate some vinyloxy radical production that is expected to be minimal. Nevertheless, vinyloxy radical and oxygen reactions were included in the model for completeness (R50–53). Oxygen mainly acts as a scavenger of ozonolysis products, particularly the C₂H₅ radical and HOCH₂CH₂ radical (R67–79). Supplementary Table 2 shows the mechanism used to model the ozonolysis reaction. These reactions are translated into a system of ordinary differential equations (ODEs) and integrated using a Bulirsch-Stoer method by the software package KINTECUS⁶³. As the dimensionless parameters shown in Supplementary Table 1 comply with the criteria by Cutler et al.⁷⁵ and Lee et al.⁷⁶ for non-Poiseuille flow, the reactor was assumed to behave reasonably close to a plug-flow reactor and modeled as a series of continuously-stirred tank reactors (CSTRs) in tandem, where the output of the previous CSTR becomes the input of a new CSTR along the flow cell. A total of 10 CSTRs were used to simulate a concentration profile along the flow cell. The use of additional segments showed convergence in the concentration profiles and, thus, only ten segments were used to facilitate simulations. A concentration profile of CH₂OO along the flow cell at different residence times is shown in Supplementary Fig. 1.

Reporting summary

Further information on research design is available in the Nature Portfolio Reporting Summary linked to this article.

Data availability

Source data are provided with this paper.

References

1. Horie, O. & Moortgat, G. K. Gas-phase ozonolysis of alkenes. Recent advances in mechanistic investigations. *Acc. Chem. Res.* **31**, 387–396 (1998).
2. Finlayson-Pitts, B. J. & Pitts, J. N. *Chemistry of the upper and lower atmosphere: theory, experiments, and applications*. 196–201 (Academic Press, 2000).
3. Atkinson, R. Atmospheric chemistry of VOCs and NO_x. *Atmos. Environ.* **34**, 2063–2101 (2000).
4. J. G. Calvert et al. *The mechanisms of atmospheric oxidation of the alkenes* (Oxford University Press, 2000).
5. Donahue, N. M., Drozd, G. T., Epstein, S. A., Presto, A. A. & Kroll, J. H. Adventures in Ozoneland: down the Rabbit-Hole. *Phys. Chem. Chem. Phys.* **13**, 10848 (2011).
6. Chen, L., Huang, Y., Xue, Y., Cao, J. & Wang, W. Competition between HO₂ and H₂O₂ reactions with CH₂OO/anti-CH₃CHOO in the oligomer formation: a theoretical perspective. *J. Phys. Chem. A* **121**, 6981–6991 (2017).
7. Sarnela, N. et al. Measurement–model comparison of stabilized Criegee intermediate and highly oxygenated molecule production in the CLOUD chamber. *Atmos. Chem. Phys.* **18**, 2363–2380 (2018).
8. Criegee, R. Mechanism of ozonolysis. *Angew. Chem. Int. Ed. Engl.* **14**, 745–752 (1975).
9. Nguyen, T. L., Lee, H., Matthews, D. A., McCarthy, M. C. & Stanton, J. F. Stabilization of the simplest criegee intermediate from the reaction between ozone and ethylene: a high-level quantum chemical and kinetic analysis of ozonolysis. *J. Phys. Chem. A* **119**, 5524–5533 (2015).

10. Wheeler, S. E., Ess, D. H. & Houk, K. N. Thinking out of the black box: accurate barrier heights of 1,3-dipolar cycloadditions of ozone with acetylene and ethylene. *J. Phys. Chem. A* **112**, 1798–1807 (2008).
11. Hatakeyama, S., Kobayashi, H., Lin, Z. Y., Takagi, H. & Akimoto, H. Mechanism for the reaction of CH₂OO with SO₂. *J. Phys. Chem.* **90**, 4131–4135 (1986).
12. Olzmann, M., Kraka, E., Cremer, D., Gutbrod, R. & Andersson, S. Energetics, kinetics, and product distributions of the reactions of ozone with ethene and 2,3-dimethyl-2-butene. *J. Phys. Chem. A* **101**, 9421–9429 (1997).
13. Hakala, J. P. & Donahue, N. M. Pressure-dependent Criegee intermediate stabilization from alkene ozonolysis. *J. Phys. Chem. A* **120**, 2173–2178 (2016).
14. Drozd, G. T. & Donahue, N. M. Pressure dependence of stabilized Criegee intermediate formation from a sequence of alkenes. *J. Phys. Chem. A* **115**, 4381–4387 (2011).
15. Welz, O. et al. Direct kinetic measurements of Criegee intermediate (CH₂OO) formed by reaction of CH₂I with O₂. *Science* **335**, 204–207 (2012).
16. Beames, J. M., Liu, F., Lu, L. & Lester, M. I. Ultraviolet spectrum and photochemistry of the simplest Criegee intermediate CH₂OO. *J. Am. Chem. Soc.* **134**, 20045–20048 (2012).
17. Ting, W.-L., Chen, Y.-H., Chao, W., Smith, M. C. & Lin, J. J.-M. The UV absorption spectrum of the simplest Criegee intermediate CH₂OO. *Phys. Chem. Chem. Phys.* **16**, 10438–10443 (2014).
18. Sheps, L. Absolute ultraviolet absorption spectrum of a Criegee intermediate CH₂OO. *J. Phys. Chem. Lett.* **4**, 4201–4205 (2013).
19. Su, Y. T., Huang, Y. H., Witek, H. A. & Lee, Y. P. Infrared absorption spectrum of the simplest Criegee intermediate CH₂OO. *Science* **340**, 174–176 (2013).
20. Fang, Y. et al. Deep tunneling in the unimolecular decay of CH₃CHOO Criegee intermediates to OH radical products. *J. Chem. Phys.* **145**, 234308 (2016).
21. Chhantyal-Pun, R., Davey, A., Shallcross, D. E., Percival, C. J. & Orr-Ewing, A. J. A kinetic study of the CH₂OO Criegee intermediate self-reaction, reaction with SO₂ and unimolecular reaction using cavity ring-down spectroscopy. *Phys. Chem. Chem. Phys.* **17**, 3617–3626 (2015).
22. Welz, O. et al. Rate coefficients of C₁ and C₂ Criegee intermediate reactions with formic and acetic acid near the collision limit: direct kinetics measurements and atmospheric implications. *Angew. Chem. Int. Ed.* **53**, 4547–4550 (2014).
23. Foreman, E. S., Kapnas, K. M. & Murray, C. Reactions between Criegee intermediates and the inorganic acids HCl and HNO₃: kinetics and atmospheric implications. *Angew. Chem. Int. Ed.* **55**, 10419–10422 (2016).
24. Buras, Z. J., Elsamra, R. M. I. & Green, W. H. Direct determination of the simplest Criegee intermediate (CH₂OO) self reaction rate. *J. Phys. Chem. Lett.* **5**, 2224–2228 (2014).
25. Buras, Z. J., Elsamra, R. M. I., Jalan, A., Middaugh, J. E. & Green, W. H. Direct kinetic measurements of reactions between the simplest Criegee intermediate CH₂OO and alkenes. *J. Phys. Chem. A* **118**, 1997–2006 (2014).
26. Pfeifle, M. et al. Nascent energy distribution of the Criegee intermediate CH₂OO from direct dynamics calculations of primary ozonide dissociation. *J. Chem. Phys.* **148**, 174306 (2018).
27. Yang, L. & Zhang, J. Effect of carbon chain length on nascent yields of stabilized Criegee intermediates in ozonolysis of a series of terminal alkenes. *J. Am. Chem. Soc.* **146**, 24591–24601 (2024).
28. Yang, L., Campos-Pineda, M. & Zhang, J. Low-pressure and nascent yields of thermalized Criegee intermediate in ozonolysis of ethene. *J. Phys. Chem. Lett.* **13**, 11496–11502 (2022).
29. Cox, R. A. et al. Evaluated kinetic and photochemical data for atmospheric chemistry: volume VII – Criegee intermediates. *Atmos. Chem. Phys.* **20**, 13497–13519 (2020).
30. Kroll, J. H., Clarke, J. S., Donahue, N. M. & Anderson, J. G. Mechanism of HO_x formation in the gas-phase ozone–alkene reaction. 1. Direct, pressure-dependent measurements of prompt OH yields. *J. Phys. Chem. A* **105**, 1554–1560 (2001).
31. Taatjes, C. A. Criegee intermediates: what direct production and detection can teach us about reactions of carbonyl oxides. *Annu. Rev. Phys. Chem.* **68**, 183–207 (2017).
32. Ahrens, J. et al. Infrared detection of Criegee intermediates formed during the ozonolysis of β-pinene and their reactivity towards sulfur dioxide. *Angew. Chem. Int. Ed.* **53**, 715–719 (2014).
33. Womack, C. C., Martin-Drumel, M. A., Brown, G. G., Field, R. W. & McCarthy, M. C. Observation of the simplest Criegee intermediate CH₂OO in the gas-phase ozonolysis of ethylene. *Sci. Adv.* **1**, e1400105 (2015).
34. Foreman, E. S. et al. High resolution absolute absorption cross sections of the B'A'–X'A' transition of the CH₂OO biradical. *Phys. Chem. Chem. Phys.* **17**, 32539–32546 (2015).
35. Mir, Z. S. et al. CH₂OO Criegee intermediate UV absorption cross-sections and kinetics of CH₂OO + CH₂OO and CH₂OO + I as a function of pressure. *Phys. Chem. Chem. Phys.* **22**, 9448–9459 (2020).
36. Robinson, G. W. & DiGiorgio, V. E. The nature of formaldehyde in its low-lying excited states. *Can. J. Chem.* **36**, 31–38 (1958).
37. Bogumil, K. et al. Measurements of molecular absorption spectra with the SCIAMACHY pre-flight model: instrument characterization and reference data for atmospheric remote-sensing in the 230–2380 nm region. *J. Photochem. Photobiol. A* **157**, 167–184 (2003).
38. Sun, C., Xu, B., Lv, L. & Zhang, S. Theoretical investigation on the reaction mechanism and kinetics of a Criegee intermediate with ethylene and acetylene. *Phys. Chem. Chem. Phys.* **21**, 16583–16590 (2019).
39. Vereecken, L., Harder, H. & Novelli, A. The reactions of criegee intermediates with alkenes, ozone, and carbonyl oxides. *Phys. Chem. Chem. Phys.* **16**, 4039 (2014).
40. Vereecken, L., Rickard, A. R., Newland, M. J. & Bloss, W. J. Theoretical study of the reactions of Criegee intermediates with ozone, alkylhydroperoxides, and carbon monoxide. *Phys. Chem. Chem. Phys.* **17**, 23847–23858 (2015).
41. Onel, L., Blitz, M., Seakins, P., Heard, D. & Stone, D. Kinetics of the gas phase reactions of the Criegee intermediate CH₂OO with O₃ and IO. *J. Phys. Chem. A* **124**, 6287–6293 (2020).
42. Copeland, G., Ghosh, M. V., Shallcross, D. E., Percival, C. J. & Dyke, J. M. A study of the ethene–ozone reaction with photoelectron spectroscopy: measurement of product branching ratios and atmospheric implications. *Phys. Chem. Chem. Phys.* **13**, 14839 (2011).
43. Chang, Y.-P., Chang, H.-H. & Lin, J. J.-M. Kinetics of the simplest Criegee intermediate reaction with ozone studied using a mid-infrared quantum cascade laser spectrometer. *Phys. Chem. Chem. Phys.* **20**, 97–102 (2018).
44. Luo, P.-L., Chen, I. Y., Khan, M. A. H. & Shallcross, D. E. Direct gas-phase formation of formic acid through reaction of Criegee intermediates with formaldehyde. *Commun. Chem.* **6**, 130 (2023).
45. Herron, J. T. & Huie, R. E. Stopped-flow studies of the mechanisms of ozone–alkene reactions in the gas phase. *Ethylene. J. Am. Chem. Soc.* **99**, 5430–5435 (1977).
46. Su, F., Calvert, J. G. & Shaw, J. H. A FT IR spectroscopic study of the ozone–ethene reaction mechanism in oxygen-rich mixtures. *J. Phys. Chem.* **84**, 239–246 (1980).
47. Niki, H., Maker, P. D., Savage, C. M. & Breitenbach, L. P. A FT-IR study of a transitory product in the gas-phase ozone–ethylene reaction. *J. Phys. Chem.* **85**, 1024–1027 (1981).
48. Horie, O. & Moortgat, G. K. Decomposition pathways of the excited criegee intermediates in the ozonolysis of simple alkenes. *Atmos. Environ.* **25A**, 1881–1896 (1991).

49. Grosjean, E., de Andrade, J. B. & Grosjean, D. Carbonyl products of the gas-phase reaction of ozone with simple alkenes. *Environ. Sci. Technol.* **30**, 975–983 (1996).
50. Neeb, P., Horie, O. & Moortgat, G. K. The ethene–ozone reaction in the gas phase. *J. Phys. Chem. A* **102**, 6778–6785 (1998).
51. Lewin, C. S. et al. Experimental evidence for the elusive ketohydroperoxide pathway and the formation of glyoxal in ethylene ozonolysis. *Chem. Commun.* **58**, 13139–13142 (2022).
52. Klippenstein, S. J. Spiers memorial lecture: theory of unimolecular reactions. *Faraday Discuss* **238**, 11–67 (2022).
53. Orr-Ewing, A. J. & Osborn, D. L. Collection on the spectroscopy, structure, and reactivity of stabilized Criegee intermediates. *J. Phys. Chem. A* **128**, 2909–2911 (2024).
54. Liu, Y., Bayes, K. D. & Sander, S. P. Measuring rate constants for reactions of the simplest Criegee intermediate (CH_2OO) by monitoring the OH radical. *J. Phys. Chem. A* **118**, 741–747 (2014).
55. Howes, N. U. M. et al. Kinetic studies of C1 and C2 Criegee intermediates with SO_2 using laser flash photolysis coupled with photoionization mass spectrometry and time-resolved UV absorption spectroscopy. *Phys. Chem. Chem. Phys.* **20**, 22218–22227 (2018).
56. Onel, L. et al. Kinetics of the gas phase reaction of the Criegee intermediate CH_2OO with SO_2 as a function of temperature. *Phys. Chem. Chem. Phys.* **23**, 19415–19423 (2021).
57. Fogler, H. S. *Elements of chemical reaction engineering*, 6 edn (Pearson Education, 2020).
58. Campos-Pineda, M. & Zhang, J. Low-pressure yields of stabilized criegee intermediates CH_3CHOO and $(\text{CH}_3)_2\text{COO}$ in ozonolysis of *Trans*-2-Butene and 2,3-Dimethyl-2-Butene. *Chem. Phys. Lett.* **683**, 647–652 (2017).
59. Campos-Pineda, M. & Zhang, J. Product yields of stabilized Criegee intermediates in the ozonolysis reactions of *Cis*-2-Butene, 2-Methyl-2-Butene, cyclopentene, and cyclohexene. *Sci. China Chem.* **61**, 850–856 (2018).
60. Yang, L., Campos-Pineda, M., Hatem, K. & Zhang, J. Low-pressure and nascent yields of stabilized Criegee intermediates CH_2OO and CH_3CHOO in ozonolysis of propene. *Phys. Chem. Chem. Phys.* **25**, 26549–26556 (2023).
61. Smith, C. A., Pope, F. D., Cronin, B., Parkes, C. B. & Orr-Ewing, A. J. Absorption cross sections of formaldehyde at wavelengths from 300 to 340 nm at 294 and 245 K. *J. Phys. Chem. A* **110**, 11645–11653 (2006).
62. Keller-Rudek, H., Moortgat, G. K., Sander, R. & Sorensen, R. The MPI-Mainz UV/VIS spectral atlas of gaseous molecules of atmospheric interest. *Earth Syst. Sci. Data* **5**, 365–373 (2013).
63. Ianni, J. C. In *Computational fluid and solid mechanics 2003* (ed K.J. Bathe) 1368–1372 (Elsevier Science Ltd., 2003).
64. Taatjes, C. A. et al. Direct measurement of Criegee intermediate (CH_2OO) reactions with acetone, acetaldehyde, and hexafluoroacetone. *Phys. Chem. Chem. Phys.* **14**, 10391–10400 (2012).
65. Ruscic, B. Active thermochemical tables: water and water dimer. *J. Phys. Chem. A* **117**, 11940–11953 (2013).
66. Chao, W., Hsieh, J. T., Chang, C. H. & Lin, J. J. M. Direct kinetic measurement of the reaction of the simplest Criegee intermediate with water vapor. *Science* **347**, 751–754 (2015).
67. Aplincourt, P. & Ruiz-López, M. F. Theoretical study of formic acid anhydride formation from carbonyl oxide in the atmosphere. *J. Phys. Chem. A* **104**, 380–388 (2000).
68. Long, B., Cheng, J.-R., Tan, X.-f & Zhang, W.-j. Theoretical study on the detailed reaction mechanisms of carbonyl oxide with formic acid. *J. Mol. Struct. Theochem* **916**, 159–167 (2009).
69. Atkinson, R. et al. Evaluated kinetic and photochemical data for atmospheric chemistry: volume i - gas phase reactions of O_x , HO_x , NO_x and SO_x species. *Atmos. Chem. Phys.* **4**, 1461–1738 (2004).
70. Atkinson, R. et al. Evaluated kinetic and photochemical data for atmospheric chemistry: volume ii – gas phase reactions of organic species. *Atmos. Chem. Phys.* **6**, 3625–4055 (2006).
71. Manion, J. A. et al. NIST chemical kinetics database, NIST standard reference database 17, version 7.0 (web version), release 1.6.8, data version 2015.09, <https://kinetics.nist.gov/> (2023).
72. Berndt, T. et al. Kinetics of the unimolecular reaction of CH_2OO and the bimolecular reactions with the water monomer, acetaldehyde and acetone under atmospheric conditions. *Phys. Chem. Chem. Phys.* **17**, 19862–19873 (2015).
73. Stone, D. et al. Unimolecular decomposition kinetics of the stabilised Criegee intermediates CH_2OO and CD_2OO . *Phys. Chem. Chem. Phys.* **20**, 24940–24954 (2018).
74. Peltola, J., Seal, P., Inkilä, A. & Eskola, A. Time-resolved, broadband UV-absorption spectrometry measurements of criegee intermediate kinetics using a new photolytic precursor: unimolecular decomposition of CH_2OO and its reaction with formic acid. *Phys. Chem. Chem. Phys.* **22**, 11797–11808 (2020).
75. Cutler, A. H., Antal, M. J. & Jones, M. A critical evaluation of the plug-flow idealization of tubular-flow reactor data. *Ind. Eng. Chem. Res.* **27**, 691–697 (1988).
76. Lee, J. C., Yetter, R. A., Dryer, F. L., Tomboulides, A. G. & Orszag, S. A. Simulation and analysis of laminar flow reactors. *Combust. Sci. Technol.* **159**, 199–212 (2000).
77. Vandaele, A. C., Hermans, C. & Fally, S. Fourier transform measurements of SO_2 absorption cross sections: II. temperature dependence in the 29000–44000 cm^{-1} (227–345 nm) region. *J. Quant. Spectrosc. Radiat. Transf.* **110**, 2115–2126 (2009).

Acknowledgements

This work was supported by the US National Science Foundation grant CHE-2155232. M.C. acknowledges support from UCMEXUS-CONACYT Doctoral Fellowship. L.Y. acknowledges support from UC Riverside Dissertation Research Grant. J.Z. acknowledges support from UC Riverside OASIS Internal Funding Award.

Author contributions

All authors conceived the project. M.C. and L.Y. developed the methodology. L.Y. and M.C. conducted experiments and kinetic simulation and performed data analysis. J.Z. supervised the project. All authors wrote the manuscript.

Competing interests

The authors declare no competing interests.

Additional information

Supplementary information The online version contains supplementary material available at <https://doi.org/10.1038/s41467-025-61739-5>.

Correspondence and requests for materials should be addressed to Jingsong Zhang.

Peer review information *Nature Communications* thanks the anonymous reviewers for their contribution to the peer review of this work. A peer review file is available.

Reprints and permissions information is available at <http://www.nature.com/reprints>

Publisher's note Springer Nature remains neutral with regard to jurisdictional claims in published maps and institutional affiliations.

Open Access This article is licensed under a Creative Commons Attribution 4.0 International License, which permits use, sharing, adaptation, distribution and reproduction in any medium or format, as long as you give appropriate credit to the original author(s) and the source, provide a link to the Creative Commons licence, and indicate if changes were made. The images or other third party material in this article are included in the article's Creative Commons licence, unless indicated otherwise in a credit line to the material. If material is not included in the article's Creative Commons licence and your intended use is not permitted by statutory regulation or exceeds the permitted use, you will need to obtain permission directly from the copyright holder. To view a copy of this licence, visit <http://creativecommons.org/licenses/by/4.0/>.

© The Author(s) 2025